THE JOURNAL OF PHYSICAL CHEMISTRY C

Article

pubs.acs.org/JPCC

Enhancing the Optical Absorption and Interfacial Properties of $BiVO_4$ with Ag_3PO_4 Nanoparticles for Efficient Water Splitting

Maged N. Shaddad,[†,§] Drialys Cardenas-Morcoso,[‡,§] Prabhakarn Arunachalam,[†] Miguel García-Tecedor,[‡] Mohamed A. Ghanem,[†] Juan Bisquert,[‡] Abdullah Al-Mayouf,[*,†] and Sixto Gimenez[*,‡]

[†]Electrochemistry Research Group, Department of Chemistry, Faculty of Science, King Saud University, Riyadh 11451, Saudi Arabia
[‡]Institute of Advanced Materials (INAM), Universitat Jaume I, 12071 Castelló, Spain

Supporting Information

ABSTRACT: Photoelectrochemical water splitting using semiconductor materials has emerged as a promising approach to produce hydrogen (H_2) from renewable resources such as sunlight and water. In the present study, Ag_3PO_4 nanoparticles were electrodeposited on $BiVO_4$ photoanodes for water splitting. A remarkable water oxidation photocurrent of 2.3 mA·cm^{-2} at 1.23 V versus reversible hydrogen electrode with ~100% Faradaic efficiency was obtained, which constitutes a notable increase compared to the pristine $BiVO_4$ photoanode. It is demonstrated that the enhancement of optical absorption (above-band gap absorbance) and the decrease of surface losses after the optimized deposition of Ag/Ag_3PO_4 nanoparticles are responsible for this notable performance. Remarkably, this heterostructure shows promising stability, demonstrating 25% decrease of photocurrent after 24 h continuous operation. This approach may open new avenues for technologically exploitable water oxidation photoanodes based on metal oxides.

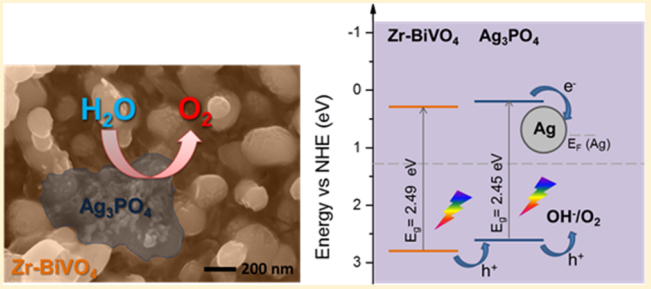

INTRODUCTION

The development of photoelectrochemical strategies for the production of added-value chemicals and fuels using solar light is particularly attractive to overcome the dependence of fossil fuels at a global scale.[1] Specifically, the photoelectrochemical oxidation of H_2O to produce solar H_2 as a clean energy vector or valuable chemical precursor stands out as one of the most promising approaches in this direction.[2] The main barrier to the full technological deployment of the technology relates to the high overpotentials needed to carry out the water oxidation reaction. In this context, coupling photoactive materials with catalytic or passivation layers is the key process to enable an efficient and stable flow of charge carriers toward the production of the desired product at the semiconductor−liquid junction. To date, the highest performance obtained (16% solar-to-hydrogen) involves the use of inverted metamorphic multijunction semiconductor architectures, interfaced with water reduction cocatalysts.[3] In these devices, the photovoltage to drive the current flow is generated inside the multijunction (buried junction), and the contact with the liquid solution is engineered with the deposition of catalytic/passivation layers to minimize the recombination losses at the interface. A more cost-effective approach entails the use of earth-abundant n-type semiconductors interfaced with catalytic/passivation layers to minimize the recombination losses at the interface. Although the achieved performance is significantly lower compared to the buried junction photoanodes, materials such as $BiVO_4$ have achieved promising efficiencies, which justify the exploration of metal oxides as candidate materials for the production of solar fuels.[4−8]

On the other hand, the best water oxidation catalysts reported to date are based on scarce and expensive materials such as IrO_2 or RuO_2, which also suffer from low stability under harsh environments, precluding large technological deployment. Consequently, during the last years, an extensive research activity targeting upscalable water oxidation catalysts has been developed. One of the most promising materials reported to date is silver phosphate, Ag_3PO_4, a semiconductor material with an indirect band gap of 2.45 eV, able to absorb light up to 500 nm in the visible region.[9,10] Its valence band minimum is located at 2.67 V versus reversible hydrogen electrode (RHE), more positive than the thermodynamic potential for water oxidation (1.23 V vs RHE).[9] Consequently, Ag_3PO_4 has the ability to oxidize H_2O to produce O_2, which makes this material an attractive candidate for photocatalytic water oxidation. The potential of Ag_3PO_4 as a functional material for photoelectrocatalytic applications was first reported by Yi et al.,[11] showing an extremely high performance for water oxidation under visible light irradiation. In particular, they reported 90% quantum efficiency for O_2 evolution with this material. However, photocorrosion of Ag_3PO_4 takes place in the absence of sacrificial reagents; therefore, the design of a photoelectrochemical cell in which the Ag_3PO_4 film acted as both

Received: January 22, 2018
Revised: April 24, 2018
Published: May 9, 2018

DOI: 10.1021/acs.jpcc.8b00738
J. Phys. Chem. C XXXX, XXX, XXX−XXX

Scheme 1. Representation of the Ag_3PO_4−(Zr)−$BiVO_4$ Photoanode Preparation: (I) Cathodic Deposition of Ag (Metal) from 0.01 M CH_3COOAg in DMSO; (II) Anodic Oxidation of the Ag Particles in Sodium Phosphate Buffer at pH 7.5; and (III) Photoelectrochemical Water Splitting on the Ag_3PO_4−(Zr)−$BiVO_4$ Surface

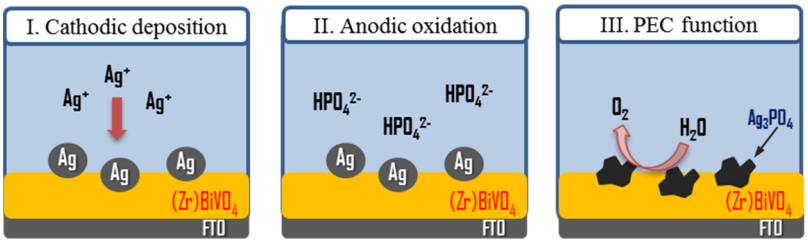

water oxidization and halting/delaying of the photocorrosion electrode was proposed by incorporating a solar cell instead of the sacrificial reagent. Ag_3PO_4-based heterojunction structures have been developed in order to enhance the charge separation of light-induced electron−hole pairs: Ag_3PO_4/TiO_2[12] and Ag_3PO_4/Fe_2O_3[13] composites, mainly for applications on photodecomposition of organic pollutants. In parallel, important efforts have been devoted to understand the effect of the crystalline structure,[14,15] particle size,[16] and morphology[17,18] of Ag_3PO_4, as well as the effect of the phosphate salts used as the precipitating agent during the synthesis, on their photocatalytic properties.[19] Several authors have reported that metallic silver at the surface of Ag_3PO_4 acts as an electron acceptor, enhancing the charge separation and preventing the decomposition of Ag_3PO_4. Additionally, it has been reported that metallic Ag improves the light-harvesting efficiency, leading to enhanced photocatalytic activity and high stability under visible light irradiation.[20−24] As an example, Chen and co-workers developed a new graphene-bridged $Ag_3PO_4/Ag/BiVO_4$ Z-scheme heterojunction showing an outstanding visible-light-driven photocatalytic performance, because of the cooperative catalytic effect of Ag/Ag_3PO_4 and reduced graphene oxide, by providing higher surface area, enhanced light-harvesting efficiency, and remarkably improved charge separation efficiency.[25] Li et al. also described the selective deposition of Ag_3PO_4 nanoparticles on highly active $BiVO_4$ (040) facets to develop an efficient heterostructured photocatalyst.[26] Inspired by these previous reports, we have synthesized Zr-doped $BiVO_4$ photoanodes decorated with Ag_3PO_4 nanoparticles for water oxidation (Ag_3PO_4−Zr−$BiVO_4$), using a novel method based on electrodeposition, achieving photocurrents of 2.3 mA·cm^{-2} at 1.23 V versus RHE and promising stability, showing ∼25% loss of photocurrent after 24 h continuous operation. This notable performance is ascribed to the optical enhancement and the decrease of surface losses produced by the dispersion of Ag_3PO_4 nanoparticles on $BiVO_4$.

■ MATERIALS AND EXPERIMENTAL METHOD

$BiVO_4$ photoanodes were synthesized through a two-step method developed by Choi et al.,[27] consisting of Bi electrodeposition on fluorine-doped tin oxide (FTO)-coated glass, followed by a reaction with the vanadium precursor. Zr was added as 2.5 mol % of $ZrCl_2O{\cdot}8H_2O$ (Sigma-Aldrich) to the Bi^{3+} plating bath, according to a previous optimization process.[28] The electrodeposition of metallic Ag was carried out from a solution of 0.01 M CH_3COOAg (Sigma-Aldrich) in DMSO. The cathodic deposition was performed potentiostatically at −2.0 V versus Ag/AgCl varying the total deposition charge (from 5 to 30 mC·cm^{-2}). In order to obtain the Ag_3PO_4 particles, the Ag−$BiVO_4$ and Ag−Zr−$BiVO_4$ films were conditioned by cyclic voltammetry scans from −0.5 to 1.6 V (vs Ag/AgCl) in a 0.1 M phosphate buffer solution at pH 7.5, at 50 mV s^{-1} scan rate. Scheme 1 in the main text illustrates the different steps of the synthetic procedure to obtain the Ag_3PO_4−(Zr)−$BiVO_4$ photoanodes.

Morphological and compositional characterization of the electrodes was studied by field emission scanning electron microscopy (SEM) with a JSM-7000F JEOL FEG-SEM system (Tokyo, Japan) equipped with an INCA 400 Oxford energy-dispersive system (EDS) analyzer (Oxford, U.K.) operating at 15 kV and a JEM-2100 JEOL transmission electron microscope (TEM) operating at 200 kV. Prior to the SEM experiment, the samples were sputtered with a 2 nm thick layer of Pt. X-ray diffraction spectra were obtained using Rigaku Miniflex 600 (Rigaku Corporation, Tokyo, Japan) with copper Kα radiation (λ = 1.5418 Å) at a scan speed of 3°·min^{-1}. Surface analysis was carried out by X-ray photoelectron spectroscopy (XPS) using the Specs SAGE 150 instrument. The analyses were performed using nonmonochrome Al Kα irradiation (1486.6 eV) at 20 mA and 13 kV, a constant energy pass of 75 eV for overall analysis, 30 eV for analysis in the specific binding energy ranges of each element, and a measurement area of 1 × 1 mm^2. The pressure in the analysis chamber was 8 × 10^{-9} hPa. The data were evaluated using CasaXPS software. The energy corrections of the spectra were performed considering a reference value of C 1s from the organic matter at 284.8 eV. The optical properties of the prepared films were also determined through UV−vis using a Cary 300 bio spectrometer. The absorbance (A) was estimated from transmittance (T) and diffuse reflectance (R) measurements using an integrating sphere as $A = -\log(T + R)$. The direct optical band gap was estimated by the Tauc plot as $(h\nu\alpha)^{1/n} = A(h\nu - E_g)$, where n = 1/2 for direct transitions.

The photoelectrochemical characterization of the electrodes was carried out by means of cyclic and linear voltammetry in the dark and under illumination (100 mW·cm^{-2}) in a 0.1 M phosphate buffer solution of pH 7.5. Alternatively, a 1 M Na_2SO_3 solution was added to the electrolyte as a hole scavenger to determine the charge separation and charge injection efficiencies. The electrochemical cell was composed by the working electrode, an Ag/AgCl (3 M KCl) reference electrode and a Pt wire as a counter electrode. All the potentials were referred to the RHE through the Nernst equation: $V_{RHE} = V_{Ag/AgCl} + V^0_{Ag/AgCl} + 0.059pH$, where $V^0_{Ag/AgCl}$(3 M KCl) = 0.21 V. All the experiments were carried out by using an AutoLab potentiostat PGSTAT302, and for those under illumination, a 300 W Xe lamp was used. The light intensity was adjusted with a thermopile to 100 mW·cm^{-2} (illumination through the substrate). Incident photon-to-current efficiency (IPCE) measurements were performed with a 150 W Xe lamp coupled with a monochromator controlled by a computer. The

DOI: 10.1021/acs.jpcc.8b00738
J. Phys. Chem. C XXXX, XXX, XXX−XXX

photocurrent was measured at 1.23 V versus RHE, with a 10 nm spectral step, using an optical power meter. IPCE was calculated through the expression $\text{IPCE}\,\% = \frac{I_{ph}(A)}{P(W)} \times \frac{1239.8}{\lambda\ (\text{nm})} \times 100$. The absorbed photon-to-current efficiency (APCE) spectra were also calculated as $\text{APCE}\,\% = \frac{\text{IPCE}}{\eta_{e^-/h^+}} \times 100$, where η_{e^-/h^+} is the absorptance, defined as the fraction of electron−hole pairs generated per incident photon flux and can be obtained from the absorbance (A) measure as $\eta_{e^-/h^+} = 1 - 10^{-A}$. In order to determine the Faradaic efficiency for O_2 evolution at the electrode surface, the amount of evolved O_2 was monitored every 5 min during a chronoamperometric measurement at 1.6 V versus RHE in phosphate buffer (pH 7.5), using a sealed cell coupled to a gas chromatograph.

RESULTS AND DISCUSSION

The overall process to deposit Ag_3PO_4 nanoparticles on (Zr)−$BiVO_4$ films is described in Scheme 1. With this electrochemical method, a good control over the amount of Ag_3PO_4 deposited on the surface of $BiVO_4$ was obtained. After the cathodic deposition of Ag on both bare and Zr-doped $BiVO_4$ films (Scheme 1, panel I), submicrometric globular metallic Ag particles (~200−400 nm diameter) can be identified on the $BiVO_4$ surface by SEM as shown in Figure 1a and confirmed by the EDS compositional analysis (Supporting Information, Figure S1). The measured lattice spacing of these globular particles (2.35 Å) by TEM (Figure 1c) is consistent with the (111) planes of the body-centered cubic structure of metallic Ag. The Ag−(Zr)−$BiVO_4$ films were then electrochemically treated (trough 15 cyclic voltammetry scans) in a sodium phosphate buffer at pH 7.5 (Scheme 1, panel II). During this electrochemical treatment, the anodic oxidation of the globular metallic Ag submicrometric particles takes place, as shown in Supporting Information, Figure S2 yielding to a significant morphological and chemical modification related to the formation of clusters around 80−100 nm diameter of 5−10 nm Ag_3PO_4 nanoparticles (Figure 1b). Although the TEM characterization did not evidence the presence of lattice fringes on the Ag_3PO_4 nanoparticles, probably because of its poor crystallinity, after the electrochemical treatment (Figure 1d), the EDS analysis (shown in Supporting Information, Figure S3) is consistent with the formation of Ag_3PO_4, as described by eq 1

$$3Ag_{(M)} + HPO_4^{2-}{}_{(aq)} \rightleftarrows Ag_3PO_{4(s)} + H^+{}_{(aq)} + 3e^- \quad (1)$$

Additionally, the XRD analysis indicates that there is no formation of new phases in the Ag_3PO_4−(Zr)−$BiVO_4$ films during this electrochemical treatment (Figure 1e). Monoclinic $BiVO_4$ was identified by the PDF card no. 00-014-0688. The slight shift on the diffraction peak corresponding to the (−121) planes of $BiVO_4$ after Zr addition is consistent with the substitutional doping previously reported, with Zr replacing Bi^{3+} positions in the lattice and increasing the carrier density of $BiVO_4$.[28] Moreover, after a detailed statistical analysis on Zr−$BiVO_4$ specimens, the identification of previously reported ZrO_2 nanoparticles was marginal, confirming that the main role of Zr in $BiVO_4$ is substitutional doping. On the other hand, it has been demonstrated that the direct lattice strain can significantly affect the intrinsic electrocatalytic property of the catalysts.[29−31] Particularly, the beneficial effects of substitutional Mo doping on $BiVO_4$ have been demonstrated to be partially derived from surface oxygen quasivacancies.[32] Consequently, it is plausible that the induced lattice strain on the $BiVO_4$ structure by substitutional Zr doping can play a significant role in the catalytic activity.

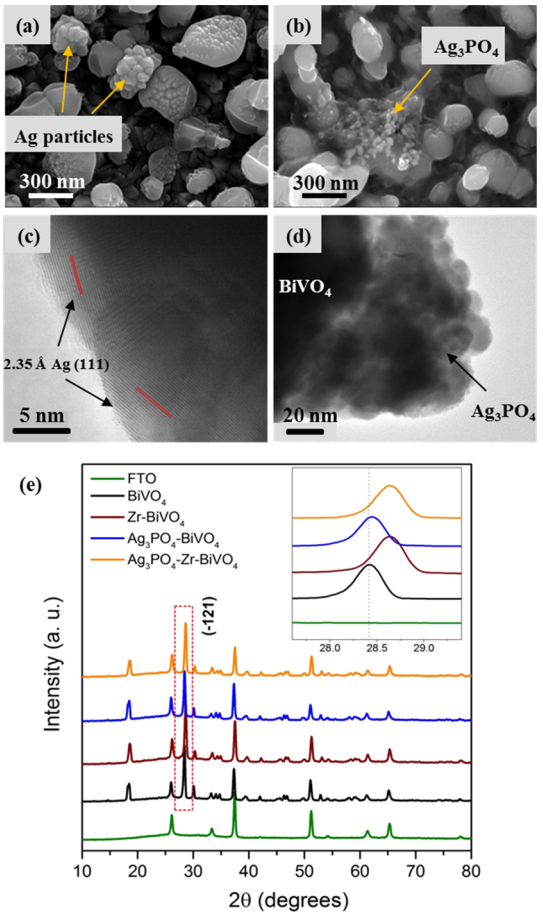

Figure 1. SEM micrographs of (a) Zr−$BiVO_4$ film showing the as-deposited Ag nanoparticles and (b) Ag_3PO_4−Zr−$BiVO_4$ photoanode obtained after 15 cycles in sodium phosphate buffer. TEM micrographs of (c) Ag−Zr−$BiVO_4$ particles showing the (111) planes corresponding to Ag particles and (d) Ag_3PO_4 nanoparticle over $BiVO_4$ in Ag_3PO_4−Zr−$BiVO_4$. (e) XRD diffractograms of the pristine and modified $BiVO_4$ films. The PDF card number for $BiVO_4$ is 00-014-0688. The inset shows a zoom of the (−121) plane of $BiVO_4$ illustrating the substitutional doping of Zr, consistent with a previous report.[28]

Further evidence of the transformation of metallic Ag into Ag_3PO_4 during the electrochemical treatment was provided by XPS. The global spectra of all the measured samples show the characteristic split signal corresponding to the Bi $4f_{5/2}$ and Bi $5f_{7/2}$ orbitals of Bi^{3+} state in $BiVO_4$ (Figure 2a), as well as the V 2p and O 1s signals corresponding to V^{5+} and O^{2-} ions, respectively. In particular, the samples containing Zr also show the characteristic Zr 3d and Zr $3p_{1/2}$ and Zr $3p_{3/2}$ signals (Figure 2b). Because the amount of Zr is at the detection limit of the equipment, the ratios between the Zr $3p_{1/2}$ and Zr $3p_{3/2}$ areas, because of the spin−orbit splitting, could not be properly analyzed. The asymmetry of the Ag 3d corresponding signal suggests the presence of different oxidation states for silver on the Ag_3PO_4−Zr−$BiVO_4$ electrode. After the deconvolution of the signal (Figure 2c), two strong signals at 373.7 and 367.4 eV are resolved, corresponding to Ag $3d_{3/2}$ and Ag $3d_{5/2}$ orbitals of

DOI: 10.1021/acs.jpcc.8b00738
J. Phys. Chem. C XXXX, XXX, XXX−XXX

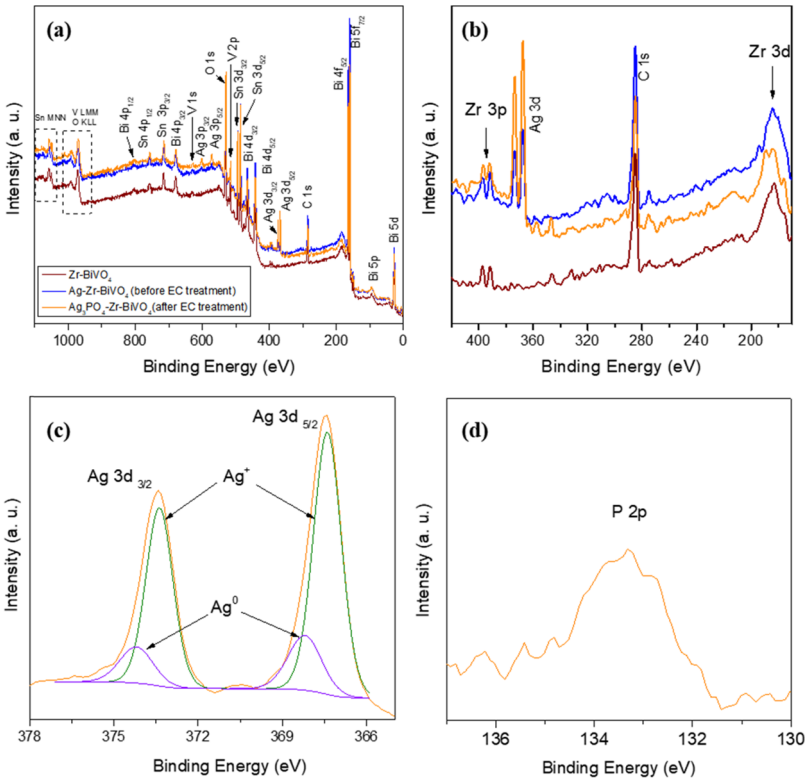

Figure 2. (a) Global XPS spectra of Zr−$BiVO_4$, Ag−Zr−$BiVO_4$, and Ag_3PO_4−Zr−$BiVO_4$ electrodes before and after electrochemical treatment, respectively. (b) Zoomed-in image showing the characteristic signals of Zr 3d and Zr 3p orbitals, (c) Ag 3d, and (d) P 2p characteristic peaks in the Ag_3PO_4−Zr−$BiVO_4$ electrode.

Ag^+, respectively. These results are consistent with previous reports,[25,26] supporting the oxidation of metallic Ag during the electrochemical treatment. However, the characteristic Ag^0 signal is also detected at 374.2 and 368.2 eV, with a weaker intensity, indicating the presence of metallic Ag. Previous studies have highlighted the beneficial effect of elemental silver Ag^0 on the surface of Ag_3PO_4, acting as an electron acceptor to enhance the charge separation and preventing the reductive decomposition of Ag_3PO_4.[33] Finally, the P 2p signal corresponding to P^{5+} in $(PO_4)^{3-}$ anion can also be identified in the spectra of the Ag_3PO_4−Zr−$BiVO_4$ electrode, as shown in Figure 2d, further supporting the formation of Ag_3PO_4. The presence of Sn in the XPS spectra (Figure 2a) is coming from the underlying FTO substrate, which is exposed at some locations because of the porous nature of the specimens.

The optical measurements shown in Figure 3a clearly demonstrate that Zr addition enhances the optical absorption (increased above-band gap absorbance) and Ag_3PO_4 increases both optical absorption (increased above-band gap absorbance) and scattering (increased absorbance at wavelengths >550 nm). Tauc plots for the determination of the band gap are shown in Supporting Information, Figure S4a. Furthermore, the additive effect of Zr and Ag_3PO_4 in the Ag_3PO_4−Zr−$BiVO_4$ spectrum is also apparent because it can be obtained as the addition of both Zr−$BiVO_4$ and Ag_3PO_4−$BiVO_4$ spectra. This is also shown in the Supporting Information, Figure S4b, where the spectra are subtracted from the pristine $BiVO_4$. Particularly, the effect of Ag/Ag_3PO_4 enhancing the optical absorbance at wavelengths below 500 nm is consistent with the reported 2.45 eV band gap of Ag_3PO_4. Additionally, previous studies have shown that Ag/Ag_3PO_4 nanoparticles induce light scattering,[34] as evidenced by the increased absorbance at wavelength >550 nm in Figure 3a.

The photoelectrochemical performance of the pristine and modified $BiVO_4$ photoanodes for water oxidation (Scheme 1, panel III) was evaluated by $j-V$ curves under chopped illumination as shown in Figure 3b. Similar results are obtained under continuous illumination conditions (Supporting Information, Figure S5). Preliminary optimization of the deposition conditions of Ag nanostructures was carried out by exploring different total charges for Ag deposition (0−30 $mC{\cdot}cm^{-2}$), as shown in Supporting Information, Figure S6. The optimized deposited charge density for the highest photocurrent was 10 $mC{\cdot}cm^{-1}$. Further explored conditions included the electrodeposition solution (water vs DMSO) and electrolyte (phosphate vs sulfate buffer solutions) (Supporting Information, Figure S7). Additionally, our deposition method showed enhanced performance compared to other reported methods such as the ionic exchange method (Supporting Information, Figure S8). The optimized Ag_3PO_4−Zr−$BiVO_4$ electrode reached a remarkable photocurrent density up to 2.3 $mA{\cdot}cm^{-2}$ at 1.23 V versus RHE, which involves a significant improvement compared to the pristine $BiVO_4$ (60 $\mu A\ cm^{-2}$) at the same potential. This constitutes one-third of the maximum current achievable by $BiVO_4$, according to its 2.4 eV band gap (7.5 $mA{\cdot}cm^{-2}$). The spectral signature of the photocurrent was obtained by IPCE measurements, shown in Figure 3c, in good correspondence with the measured photocurrents shown in Figure 3b. The quantitative correlation was carried out by the integration of IPCE with the solar spectrum to calculate the total photocurrent and the values included in Supporting Information, Table S1 are in excellent agreement with those obtained by voltammetry measurements, Figure 3b. From this result, it is clear that the photocurrent is mostly related to above-band gap absorbance and the absorbance at wavelength

DOI: 10.1021/acs.jpcc.8b00738
J. Phys. Chem. C XXXX, XXX, XXX−XXX

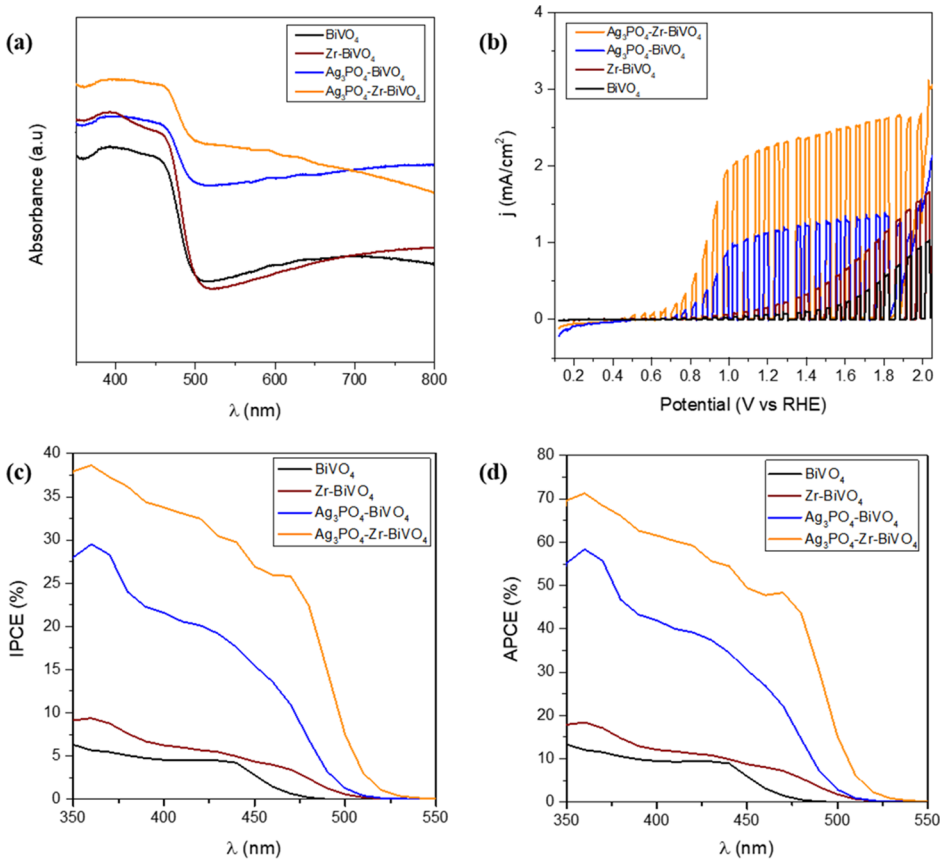

Figure 3. (a) UV−vis absorption spectra of the prepared films, (b) $j-V$ curves of the synthetized films under chopped illumination at 100 mW·cm^{-2} in phosphate buffer solution at pH 7.5, with a scan rate of 5 mV s^{-1}. (c) IPCE spectra obtained on the synthetized films at 1.23 V vs RHE in phosphate buffer solution at pH 7.5. (d) APCE spectra obtained from IPCE and absorbance measurements.

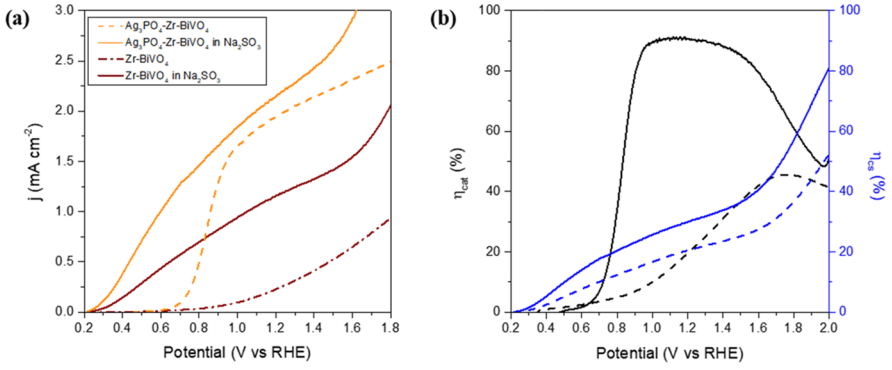

Figure 4. (a) $j-V$ curves of Ag_3PO_4−Zr−$BiVO_4$ photoanode obtained under chopped illumination at 100 mW·cm^{-2} in phosphate buffer solution at pH 7.5 and with a sacrificial hole scavenger (1 M Na_2SO_3) in the solution. (b) Charge separation efficiency and catalytic efficiency of Ag_3PO_4−Zr−$BiVO_4$ (solid lines) and Zr−$BiVO_4$ electrodes (dashed lines).

>550 nm does not contribute significantly to the photocurrent. Notably, the optical enhancement shown in Figure 3a for Zr and Ag additions is reflected on the 100 nm red shift for the photocurrent onset in the IPCE measurements. The APCE was also calculated, and the obtained results (Figure 3d) show significantly higher values compared to IPCE. This means that ∼50−70% of the photogenerated carriers are successfully extracted for water oxidation in the optimized Ag_3PO_4−Zr−$BiVO_4$ photoanode.

Further mechanistic insights to elucidate the origin of the enhanced performance of the Ag_3PO_4−Zr−$BiVO_4$ photoanodes were extracted from voltammetry measurements in the presence of a Na_2SO_3 sacrificial hole scavenger, see Figure 4a. From these measurements and the theoretical maximum photocurrent (see Supporting Information, Table S2) estimated from the absorbance measurements ($j_{abs} = \frac{e}{hc}\int \lambda \cdot I(\lambda) \cdot (1 - 10^{-A})\, d\lambda$, with $I(\lambda)$ the spectral irradiance, e the elemental charge, h the Planck constant, and c the light speed), we estimated the bulk and surface losses in the electrode by monitoring the charge separation efficiency (η_{cs}) and the charge injection efficiency (η_{cat}), defined by eqs 2 and 3

$$j_{H_2O} = j_{abs} \cdot \eta_{cs} \cdot \eta_{cat} \quad (2)$$

DOI: 10.1021/acs.jpcc.8b00738
J. Phys. Chem. C XXXX, XXX, XXX−XXX

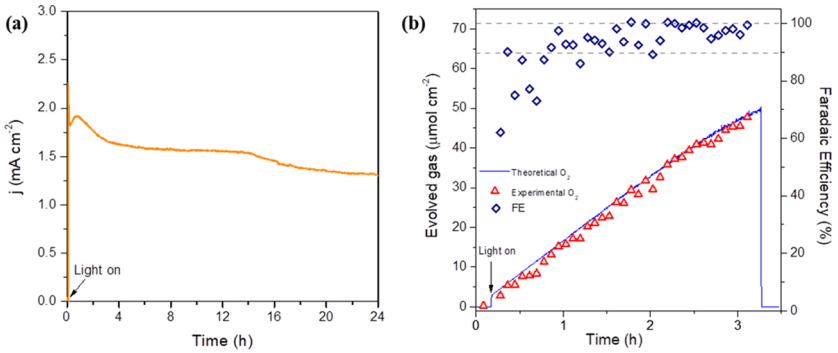

Figure 5. (a) Chronoamperometric measurement at 1.6 V vs RHE to assess the stability of the Ag_3PO_4−Zr−$BiVO_4$ electrodes in 24 h, tested under illumination at 100 mW·cm^{-2} in phosphate buffer solution at pH 7.5. (b) Oxygen evolution detected by gas chromatography and Faradaic efficiency.

$$j_{HS} = j_{abs} \cdot \eta_{cs} \quad (3)$$

In the presence of the hole scavenger, the photocurrent onset is cathodically shifted to ∼0.2 V versus RHE, which agrees well with the reported flat band potential of $BiVO_4$.[28] Additionally, the enhanced photocurrent of Ag_3PO_4−Zr−$BiVO_4$ is consistent with the higher above-band gap absorbance shown in Figure 3a. Figure 4b shows the charge separation and charge injection efficiencies for Zr−$BiVO_4$ photoanodes with and without Ag_3PO_4 nanoparticles. Remarkably, the low charge injection efficiency of pristine $BiVO_4$ (<20%) is boosted up to 90% (1−1.5 V vs RHE), in a 400 mV voltage window, highlighting the beneficial role of Ag_3PO_4 nanoparticles on the catalytic properties of the developed photoanode. Additionally, a slight increase of the charge separation efficiency is observed upon deposition of Ag_3PO_4, which is consistent with the previous reports on Ag/Ag_3PO_4/TiO_2 heterostructures, which showed better charge separation by the decreased steady-state photoluminescence of TiO_2 nanotubes upon deposition of Ag/Ag_3PO_4 nanoparticles.[34]

A durability test was carried out on the optimized Ag_3PO_4−Zr−$BiVO_4$ electrode, showing promising stability up to 24 h (Figure 5a). This can be explained by the role of the Ag/Ag_3PO_4 heterostructure, enhancing the charge separation. Because the conduction band of Ag_3PO_4 is more negative than the Fermi level of elemental Ag, electron transfer from Ag_3PO_4 to metallic silver takes place (see Supporting Information, Figure S9), hindering self-reduction, as reported elsewhere.[21,24] Further insights into the degradation mechanism were obtained by interrupting the chronoamperometric measurement every 5 h. The j−V curves under illumination were measured and optical micrographs of the electrode were taken after each time interval. The results are shown in Supporting Information, Figures S10−S12. The gradual decrease of the photocurrent can be ascribed to the overall mechanical degradation of the film, with preferential detachment of the Ag/Ag_3PO_4 nanoparticles, as evidenced by the disappearance of the Ag^+/Ag^0 peak in the j−V curves in Figure S10b. Postmortem SEM analysis after 24 h measurement also showed some smoothing of the surface of the electrode by photocorrosion (Supporting Information, Figure S12), which is consistent with $BiVO_4$ deactivation to Bi_2O_3 as previously reported.[35] Figure 5b shows the theoretical and experimental oxygen evolution during the chronoamperometric measurement, together with the Faradaic efficiency. Remarkably, almost 100% Faradaic efficiency was obtained after 3 h measurement. The scattering on the calculated values are related to the manual sampling process.

Moreover, the stability of the Ag_3PO_4−Zr−$BiVO_4$ electrode was also tested in a borate buffer at pH 9.2 as an electrolyte (Supporting Information, Figure S13). A fast decay of the current density is observed during the first 2 h of operation, which suggests that probably the Ag_3PO_4 nanoparticles are fully removed from the surface, making these conditions not suitable for further studies.

Comparing to other studied water oxidation catalysts such as Co−Pi,[36] FeOOH−NiOOH,[4] Co−Fe Prussian blue,[35] and Fe_2O_3 nanoparticles,[28] Ag/Ag_3PO_4 provides enhanced light-harvesting efficiency, which is a strong asset for achieving photoanodes with high photocurrents. Additionally, together with Co−Fe Prussian blue, and FeOOH−NiOOH, its promising stability may provide a technologically exploitable solution of water oxidation photoanodes based on metal oxides. A detailed review of the performance and stability of photoanodes based on $BiVO_4$ reported in the last three years is included in Supporting Information, Table S3. In the light of these reports, the results obtained in the present study can be properly contextualized. In particular, for photoanodes without a hole mirror layer (SnO_2, TiO_2 or WO_3), our photocurrents are competitive with the most advanced system reported. In terms of stability, only very few studies report chronoamperometric measurements beyond 4 h; consequently, the reported 25% photocurrent loss can be considered as a promising result.

CONCLUSIONS

In summary, Ag_3PO_4−Zr−$BiVO_4$ heterostructures have demonstrated competitive performance for water oxidation, with notable photocurrents of 2.3 mA·cm^{-2} at 1.23 V versus RHE and Faradaic efficiency ∼100%, promising stability, and ∼25% photocurrent loss after 24 h of operation. This behavior stems from the synergistic optical enhancement due to both Zr doping and Ag deposition, reflected as increased above-band gap absorbance, 100 nm red shift of the photocurrent onset in IPCE measurements, and the significant reduction of surface losses as evidenced by the notable increase of the catalytic efficiency up to 90%. Incremental optimization of the performance and stability of this heterostructure may provide a technologically exploitable solution of water oxidation photoanodes based on metal oxides.

ASSOCIATED CONTENT

Supporting Information

The Supporting Information is available free of charge on the ACS Publications website at DOI: 10.1021/acs.jpcc.8b00738.

DOI: 10.1021/acs.jpcc.8b00738
J. Phys. Chem. C XXXX, XXX, XXX−XXX

EDS analysis, cyclic voltammetry measurements showing the formation of the Ag_3PO_4 nanoparticles, $j-V$ curves of the different tested samples under continuous illumination, optimization of the deposition method for the Ag_3PO_4 nanoparticles, tables with the integrated currents from IPCE, and optical absorption measurements. Review of performance indicators for $BiVO_4$-based photoanodes in the last three years (PDF)

AUTHOR INFORMATION

Corresponding Authors

*E-mail: amayouf@ksu.edu.sa (A.A.-M.).
*E-mail: sjulia@uji.es (S.G.).

ORCID

Juan Bisquert: 0000-0003-4987-4887
Sixto Gimenez: 0000-0002-4522-3174

Author Contributions

§M.N.S. and D.C.-M. have equally contributed to this work.

Notes

The authors declare no competing financial interest.

ACKNOWLEDGMENTS

We would like to acknowledge the financial support from the Deanship of Scientific Research at King Saud University for funding this Research group no. RG-1438-001 and the University Jaume I through the P11B2014-51 and SOLENPE UJI-B2016-05 and to the Generalitat Valenciana through the Santiago Grisolia Program, grant 2015-031. Serveis Centrals at UJI (SCIC) are also acknowledged.

REFERENCES

(1) Montoya, J. H.; Seitz, L. C.; Chakthranont, P.; Vojvodic, A.; Jaramillo, T. F.; Nørskov, J. K. Materials for Solar Fuels and Chemicals. *Nat. Mater.* **2017**, *16*, 70−81.

(2) Walter, M. G.; Warren, E. L.; McKone, J. R.; Boettcher, S. W.; Mi, Q.; Santori, E. A.; Lewis, N. S. Solar Water Splitting Cells. *Chem. Rev.* **2010**, *110*, 6446−6473.

(3) Young, J. L.; Steiner, M. A.; Döscher, H.; France, R. M.; Turner, J. A.; Deutsch, T. G. Direct Solar-to-Hydrogen Conversion Via Inverted Metamorphic Multi-Junction Semiconductor Architectures. *Nat. Energy* **2017**, *2*, 17028.

(4) Kim, T. W.; Choi, K.-S. Nanoporous $BiVO_4$ Photoanodes with Dual-Layer Oxygen Evolution Catalysts for Solar Water Splitting. *Science* **2014**, *343*, 990−994.

(5) Abdi, F. F.; Han, L.; Smets, A. H. M.; Zeman, M.; Dam, B.; van de Krol, R. Efficient Solar Water Splitting by Enhanced Charge Separation in a Bismuth Vanadate-Silicon Tandem Photoelectrode. *Nat. Commun.* **2013**, *4*, 2195.

(6) Shi, X.; Zhang, K.; Shin, K.; Ma, M.; Kwon, J.; Choi, I. T.; Kim, J. K.; Kim, H. K.; Wang, D. H.; Park, J. H. Unassisted Photoelectrochemical Water Splitting Beyond 5.7% Solar-to-Hydrogen Conversion Efficiency by a Wireless Monolithic Photoanode/Dye-Sensitised Solar Cell Tandem Device. *Nano Energy* **2015**, *13*, 182−191.

(7) Pihosh, Y.; Turkevych, I.; Mawatari, K.; Uemura, J.; Kazoe, Y.; Kosar, S.; Makita, K.; Sugaya, T.; Matsui, T.; Fujita, D.; et al. Photocatalytic Generation of Hydrogen by Core-Shell $WO_3/BiVO_4$ Nanorods with Ultimate Water Splitting Efficiency. *Sci. Rep.* **2015**, *5*, 11141.

(8) Lamm, B.; Trześniewski, B. J.; Döscher, H.; Smith, W. A.; Stefik, M. Emerging Postsynthetic Improvements of $BiVO_4$ Photoanodes for Solar Water Splitting. *ACS Energy Lett.* **2018**, *3*, 112−124.

(9) Huang, G.-F.; Ma, Z.-L.; Huang, W.-Q.; Tian, Y.; Jiao, C.; Yang, Z.-M.; Wan, Z.; Pan, A. Semiconductor Photocatalyst: Possibilities and Challenges. *J. Nanomater.* **2013**, *2013*, 1.

(10) Pan, J.; Liu, G. Facet Control of Photocatalysts for Water Splitting. In *Semiconductors and Semimetals*; Mi, Z., Wang, L., Jagadish, C., Eds.; Elsevier, 2017; Chapter 10, Vol. *97*, pp 349−391.

(11) Yi, Z.; Ye, J.; Kikugawa, N.; Kako, T.; Ouyang, S.; Stuart-Williams, H.; Yang, H.; Cao, J.; Luo, W.; Li, Z.; et al. An Orthophosphate Semiconductor with Photooxidation Properties under Visible-Light Irradiation. *Nat. Mater.* **2010**, *9*, 559−564.

(12) Rawal, S. B.; Sung, S. D.; Lee, W. I. Novel Ag_3PO_4/TiO_2 Composites for Efficient Decomposition of Gaseous 2-Propanol under Visible-Light Irradiation. *Catal. Commun.* **2012**, *17*, 131−135.

(13) Febiyanto; Eliani, I. V.; Riapanitra, A.; Sulaeman, U. Synthesis and Visible Light Photocatalytic Properties of Iron Oxide-Silver Orthophosphate Composites. *AIP Conf. Proc.* **2015**, *1725*, 020021.

(14) Bi, Y.; Ouyang, S.; Umezawa, N.; Cao, J.; Ye, J. Facet Effect of Single-Crystalline Ag_3PO_4 Sub-Microcrystals on Photocatalytic Properties. *J. Am. Chem. Soc.* **2011**, *133*, 6490−6492.

(15) Wang, J.; Teng, F.; Chen, M.; Xu, J.; Song, Y.; Zhou, X. Facile Synthesis of Novel Ag_3PO_4 Tetrapods and the {110} Facets-Dominated Photocatalytic Activity. *CrystEngComm* **2013**, *15*, 39−42.

(16) Dinh, C.-T.; Nguyen, T.-D.; Kleitz, F.; Do, T.-O. Large-Scale Synthesis of Uniform Silver Orthophosphate Colloidal Nanocrystals Exhibiting High Visible Light Photocatalytic Activity. *Chem. Commun.* **2011**, *47*, 7797−7799.

(17) Khan, A.; Qamar, M.; Muneer, M. Synthesis of Highly Active Visible-Light-Driven Colloidal Silver Orthophosphate. *Chem. Phys. Lett.* **2012**, *519*, 54−58.

(18) Dong, P.; Wang, Y.; Li, H.; Li, H.; Ma, X.; Han, L. Shape-Controllable Synthesis and Morphology-Dependent Photocatalytic Properties of Ag_3PO_4 Crystals. *J. Mater. Chem. A* **2013**, *1*, 4651−4656.

(19) Amornpitoksuk, P.; Intarasuwan, K.; Suwanboon, S.; Baltrusaitis, J. Effect of Phosphate Salts (Na_3PO_4, Na_2HPO_4, and NaH_2PO_4) on Ag_3PO_4 Morphology for Photocatalytic Dye Degradation under Visible Light and Toxicity of the Degraded Dye Products. *Ind. Eng. Chem. Res.* **2013**, *52*, 17369−17375.

(20) Lin, X.; Hou, J.; Jiang, S.; Lin, Z.; Wang, M.; Che, G. A Z-Scheme Visible-Light-Driven $Ag/Ag_3PO_4/Bi_2MoO_6$ Photocatalyst: Synthesis and Enhanced Photocatalytic Activity. *RSC Adv.* **2015**, *5*, 104815−104821.

(21) Huang, K.; Lv, Y.; Zhang, W.; Sun, S.; Yang, B.; Chi, F.; Ran, S.; Liu, X. One-Step Synthesis of Ag_3PO_4/Ag Photocatalyst with Visible-Light Photocatalytic Activity. *Mater. Res.* **2015**, *18*, 939−945.

(22) Gondal, M. A.; Chang, X.; Sha, W. E. I.; Yamani, Z. H.; Zhou, Q. Enhanced Photoactivity on Ag/Ag_3PO_4 Composites by Plasmonic Effect. *J. Colloid Interface Sci.* **2013**, *392*, 325−330.

(23) Liu, Y.; Fang, L.; Lu, H.; Liu, L.; Wang, H.; Hu, C. Highly Efficient and Stable Ag/Ag3PO4 Plasmonic Photocatalyst in Visible Light. *Catal. Commun.* **2012**, *17*, 200−204.

(24) Li, Q.; Wang, F.; Hua, Y.; Luo, Y.; Liu, X.; Duan, G.; Yang, X. Deposition-Precipitation Preparation of $Ag/Ag_3PO_4/WO_3$ Nanocomposites for Efficient Visible-Light Degradation of Rhodamine B under Strongly Acidic/Alkaline Conditions. *J. Colloid Interface Sci.* **2017**, *506*, 207−216.

(25) Chen, F.; Yang, Q.; Li, X.; Zeng, G.; Wang, D.; Niu, C.; Zhao, J.; An, H.; Xie, T.; Deng, Y. Hierarchical Assembly of Graphene-Bridged $Ag_3PO_4/Ag/BiVO_4$ (040) Z-Scheme Photocatalyst: An Efficient, Sustainable and Heterogeneous Catalyst with Enhanced Visible-Light Photoactivity Towards Tetracycline Degradation under Visible Light Irradiation. *Appl. Catal., B* **2017**, *200*, 330−342.

(26) Li, C.; Zhang, P.; Lv, R.; Lu, J.; Wang, T.; Wang, S.; Wang, H.; Gong, J. Selective Deposition of Ag_3PO_4 on Monoclinic $BiVO_4$(040) for Highly Efficient Photocatalysis. *Small* **2013**, *9*, 3951−3956.

(27) Kang, D.; Park, Y.; Hill, J. C.; Choi, K.-S. Preparation of Bi-Based Ternary Oxide Photoanodes $BiVO_4$, Bi_2WO_6, and $Bi_2Mo_3O_{12}$ Using Dendritic Bi Metal Electrodes. *J. Phys. Chem. Lett.* **2014**, *5*, 2994−2999.

DOI: 10.1021/acs.jpcc.8b00738
J. Phys. Chem. C XXXX, XXX, XXX−XXX

(28) Shaddad, M. N.; Ghanem, M. A.; Al-Mayouf, A. M.; Gimenez, S.; Bisquert, J.; Herraiz-Cardona, I. Cooperative Catalytic Effect of ZrO_2 and α-Fe_2O_3 Nanoparticles on $BiVO_4$ Photoanodes for Enhanced Photoelectrochemical Water Splitting. *Chemsuschem* **2016**, *9*, 2779−2783.
(29) Zhang, S.; Huang, Z.; Wen, Z.; Zhang, L.; Jin, J.; Shahbazian-Yassar, R.; Yang, J. Local Lattice Distortion Activate Metastable Metal Sulfide as Catalyst with Stable Full Discharge−Charge Capability for Li−O_2 Batteries. *Nano Lett.* **2017**, *17*, 3518−3526.
(30) Feng, X.; Jiang, K.; Fan, S.; Kanan, M. W. Grain-Boundary-Dependent CO_2 Electroreduction Activity. *J. Am. Chem. Soc.* **2015**, *137*, 4606−4609.
(31) Bhatt, M. D.; Lee, J. S. Recent Theoretical Progress in the Development of Photoanode Materials for Solar Water Splitting Photoelectrochemical Cells. *J. Mater. Chem. A* **2015**, *3*, 10632−10659.
(32) Ding, K.; Chen, B.; Fang, Z.; Zhang, Y.; Chen, Z. Why the Photocatalytic Activity of Mo-Doped $BiVO_4$ Is Enhanced: A Comprehensive Density Functional Study. *Phys. Chem. Chem. Phys.* **2014**, *16*, 13465−13476.
(33) Teng, W.; Li, X.; Zhao, Q.; Zhao, J.; Zhang, D. In Situ Capture of Active Species and Oxidation Mechanism of Rhb and Mb Dyes over Sunlight-Driven Ag/Ag_3PO_4 Plasmonic Nanocatalyst. *Appl. Catal., B* **2012**, *125*, 538−545.
(34) Teng, W.; Li, X.; Zhao, Q.; Chen, G. Fabrication of Ag/Ag_3PO_4/TiO_2 Heterostructure Photoelectrodes for Efficient Decomposition of 2-Chlorophenol under Visible Light Irradiation. *J. Mater. Chem. A* **2013**, *1*, 9060−9068.
(35) Hegner, F. S.; Herraiz-Cardona, I.; Cardenas-Morcoso, D.; López, N.; Galán-Mascarós, J.-R.; Gimenez, S. Cobalt Hexacyanoferrate on BiVO4 Photoanodes for Robust Water Splitting. *ACS Appl. Mater. Interfaces* **2017**, *9*, 37671−37681.
(36) Zhong, D. K.; Choi, S.; Gamelin, D. R. Near-Complete Suppression of Surface Recombination in Solar Photoelectrolysis by "Co-Pi" Catalyst-Modified W: BiVO4. *J. Am. Chem. Soc.* **2011**, *133*, 18370−18377.

DOI: 10.1021/acs.jpcc.8b00738
J. Phys. Chem. C XXXX, XXX, XXX−XXX